

# Vibration Isolator Carrying Atomic Force Microscope's Head

Shingo Ito, Severin Unger, Georg Schitter

*Christian Doppler Laboratory for Precision Engineering for Automated In-Line Metrology,  
Automation and Control Institute (ACIN), TU Wien, Gusshausstrasse 27-29, 1040 Vienna, Austria  
(email: {ito, unger, schitter}@acin.tuwien.ac.at)*

---

## Abstract

For high-resolution imaging in harsh environments this paper proposes a vibration isolation system that actively positions the head of an atomic force microscope (AFM) to maintain the vertical distance to the sample. On the moving platform carrying the AFM head, a displacement sensor is installed to detect the vibrations between the probe and the sample that impair the imaging quality. The detected vibrations are rejected by vertically moving the platform with feedback control. For the motion, flexure-guided Lorentz actuators are designed, such that the resulting suspension mode occurs around the major spectrum of the floor vibrations. By feedback control design, the high gain of the suspension mode is used to increase the open-loop gain for better vibration rejection. The experimental results demonstrate that the vibration isolation system can reject 99.3 % of the vibrations. As a result, AFM imaging of nanoscale features is successfully performed in a vibrational environment.

*Keywords:* Atomic force microscopy, Vibration isolation, Voice coil actuators, Dual stage actuator

---

## 1. Introduction

Atomic force microscopes (AFMs) are high-resolution imaging systems to measure surface characteristics of samples [1]. To achieve the high resolution, AFMs use a probe with a sharp tip to scan the sample surface while the probe's vertical (Z-axis) motion is typically regulated to maintain the tip-sample distance or the probe deflection (i.e. constant force mode) by means of actuators with feedback control [2]. The required precision of the probe motion is nanometer or even sub-nanometer, and AFMs are typically sensitive to vibrations transmitted from the floor [3]. Such floor vibrations are caused by people and appliances (e.g. air compressors) on the floor, as well as by the traffic near the building [4–6]. Floor vibrations can fluctuate the distance between the probe and the sample, impairing the AFM imaging quality. Therefore, AFMs are typically used in quiet places and require remedies against the floor vibrations.

One of the major remedies is external vibration isolators, where their tabletop mounting AFMs is decoupled from the vibrating floor. In the case of passive vibration isolators, the tabletop is supported by mechanical components modeled as a combination of a spring and damper [7]. The problem of passive isolators is that the vibrations are transmitted through the spring to the tabletop at frequencies lower than the suspension mode's natural frequency [8]. The worst case occurs at that frequency, where the floor vibrations are amplified by the

*Preprint submitted to IFAC Mechatronics*

*April 7, 2017*

suspension resonance on the tabletop. To prevent this, the frequency is usually decreased by using a heavy and large tabletop. In the case of active vibration isolators, the tabletop motion is regulated based on the vibrations measured by sensors, and their size can be small [9]. Even with these isolators, however, the vibration isolation performance degrades at low frequencies, where the signal-to-noise ratio of the vibration sensors (e.g. accelerometer or geophones [10]) decreases [11].

The residual vibrations of an external vibration isolator can degrade the imaging quality of an AFM on it. When mechanical resonances of the AFM are excited by the residual vibrations, they change the AFM probe's position with respect to the sample, and artifacts are created in an AFM image. In order to avoid it, resonant frequencies of the AFM need to be sufficiently higher than the major spectrum of the vibrations [12]. Such a design is realized by small and rigid components for a short and rigid mechanical loop from the probe to the sample [1, 12]. However, because the components include the mechanical supports of the AFM head with the probe above the sample, the rigid AFM design restricts the sample size. This is problematic to measure large samples (e.g. CD/DVD/Blu-ray disks and wafers [1]). A practical challenge of large samples is that they may have a relatively large height variation dependent on types, and a mechanism adjusting the sample's vertical position is desired for the probe engagement (cf. Section 3.7). Such a mechanism may decrease the stiffness of the AFM system and may be excited by floor vibrations.

In order to mitigate the above problem, a high-precision displacement sensor [13] is used to measure the distance between the probe and the sample as vibrations, which has an advantage of a high signal-to-noise ratio, even at 0 Hz. The measured vibrations are used for compensation to generate vibration-free AFM images [14–16]. In the case of the AFM [17], the vibrations are actively rejected by its Z-axis actuators, and high vibration rejection performance is realized by the actuator selection, as well as the mechanical and control design. However, the Z-axis actuation is fully devoted to maintain the distance between the probe and the sample for the active rejection, and the sample topography is imaged directly from the output signal of the AFM probe used as a tip-sample displacement sensor (cf. constant height mode [2]). Consequently, the height of the sample topography that can be imaged is strictly limited by the probe's measurement range, and the AFM probe needs to be calibrated for imaging [1].

For high-performance vibration rejection and isolation without the measurement height limitation and the probe calibration, this paper proposes a vibration isolation system integrated in an AFM, where the AFM probe is vertically moved by two different types of actuators. As commonly done in AFMs, the first type of actuators serves for AFM imaging in the constant force mode for topography measurement [1]. In contrast, the second type of actuators is selected and controlled specifically for vibration rejection and isolation. This enables AFM imaging in a harsh environment despite a relatively long mechanical loop from the probe to the sample, which is ideal for large AFM samples.

For a single-axis actuation, two different types of actuators are often combined to complement each other as a dual stage actuator (DSA) [18]. In the case of AFMs, DSAs are mainly applied to realize high-speed long-range actuation [19–22]. Different from these realizations, the proposed AFM system in this paper uses two types of actuators for imaging, as well as for vibration isolation and rejection. Note that the paper focuses on the rejection and isolation of the vibrations transmitted from the floor. Other disturbances (e.g. acoustic vibrations

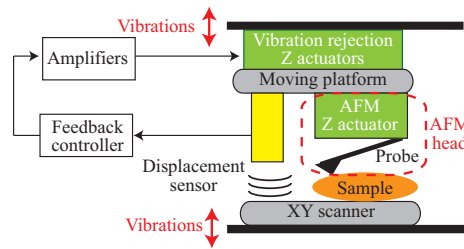


Figure 1: Illustration of the proposed vibration isolation system integrated in an AFM.

and thermal drift [1]) are not targeted in this paper.

The rest of the paper is organized as follows. Section 2 introduces the overall architecture of the proposed isolation system. The detailed component selection and system design are presented in Section 3. The isolation system is modeled in Section 4 for feedback control design and analysis in Section 5. In Section 6, the system is experimentally evaluated, and AFM imaging is demonstrated. Section 7 concludes this paper.

## 2. System concept, architecture and requirements

### 2.1. System concept and architecture

Fig. 1 illustrates the proposed vibration isolation system integrated in an AFM. The moving platform is suspended and vertically moved by Lorentz actuators (AVA-1-20-0.5, Akribis Systems, Singapore) specifically for vibration isolation and rejection. On the moving platform, a displacement sensor (ATW-01/ATP-A20, Unipulse, Tokyo, Japan) and an AFM head (afm+, Anasys, Santa Barbara, USA) are installed. The conventional AFM head has a separate piezo as a Z-axis actuator to maintain the deflection or tip-sample distance of the AFM probe. Additionally, the head includes components for the probe deflection measurement [1]. A commercial XY scanner (NPXY100-100, nPoint, Middleton, USA) scans the AFM sample. For AFM imaging, the data acquisition system of the AFM head is used.

The displacement sensor measures the distance to the XY scanner to detect the vibrations between the AFM head and the sample. By using the sensor output and feedback control, the vibration-rejection actuators regulate the moving platform position with respect to the XY scanner, such that the vibrations are rejected for vibration-free AFM imaging. To demonstrate the vibration-free AFM imaging, the proposed system is placed on a standard laboratory table, without any other external vibration isolator. The laboratory is located on the fourth floor of a building (i.e. without any vibration isolation measures). In order to determine the requirements of the system, the floor vibrations are evaluated in the next section. Afterwards, the component selection and the system design are discussed in detail.

### 2.2. Evaluation of floor vibrations

For the evaluation of the vibrations to be rejected, a geophone (SM-7/U-B, ION, Houston, USA), which has a constant sensitivity approximately between 10 Hz and 340 Hz, is placed on the laboratory table. Fig. 2(top) shows the measured vibrations fluctuating within a range

of  $\pm 100 \mu\text{m/s}$ . From the data in the time domain, the root mean square (RMS) of the vibrations filtered by a one-third octave band-pass filter is approximated (cf. [23]), as shown in Fig. 2(bottom). The plot shows that the major frequency components of the vibrations are up to about 150 Hz. Particularly below 30 Hz, large vibrations of more than  $20 \mu\text{m/s}_{\text{rms}}$  are visible. According to the generic vibration criterion [3], vibrations are desired to be less than  $6.25 \mu\text{m/s}_{\text{rms}}$  between 1 Hz and 80 Hz for typical high-resolution imaging systems.

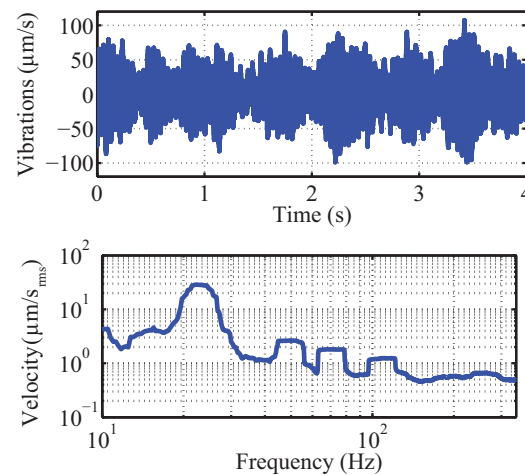


Figure 2: Floor vibrations measured by a geophone in the time domain and the approximated root mean square with the one-third octave band.

### 2.3. Requirements

As evaluated in the previous section, the vibrations show frequency components up to 150 Hz. Thus, the control bandwidth of the moving platform for the vibration rejection needs to be 150 Hz or more. In order to realize this, the displacement sensor and the amplifiers for the vibration rejection actuators need to have a sufficiently small phase lag and a short delay. By considering that a phase margin of 40-60 degrees is typically desired for closed-loop stability [7], their phase lag should be less than a few degrees at least around 150 Hz. If the frequency response of the sensor and the actuators' amplifiers are approximated by a first-order low-pass filter, a bandwidth of several kilohertz or more is required for these components.

Additionally, since the vibrations have a high amplitude less than 30 Hz in Fig. 2, it is desired to increase the vibration rejection performance in that frequency range in the mechatronic system design. Based on the requirements described above, the design of the vibration isolation system is presented in the next section.

## 3. System design

### 3.1. Moving platform

In high-precision motion control, one of the major factors that limit control bandwidth is parasitic dynamics or internal modes of mechanical systems [24]. Thus, to increase their



frequencies for a sufficient control bandwidth, a relatively thick aluminum plate of 12 mm is selected as the base plate of the moving platform as shown in Fig. 3, where the Z axis indicates the actuation direction. The base plate has a space of 84 mm × 105 mm, where the AFM head is placed on top or attached on the bottom dependent on the types.

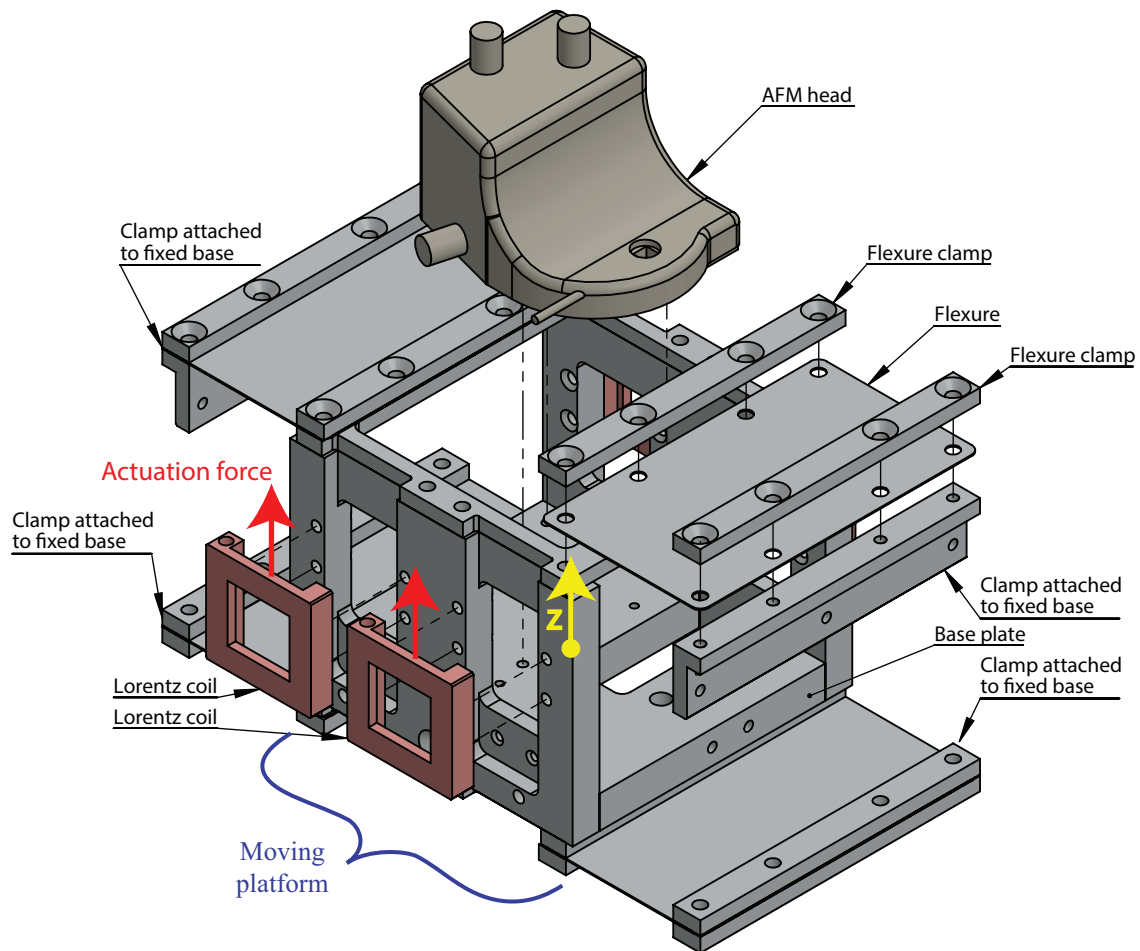


Figure 3: 3D model of the flexure-guided moving platform with moving coils of Lorentz actuators. Its simplified illustration is shown in Fig. 7.

### 3.2. Vibration rejection actuators

In order to position the moving platform with nanometer resolution, basically two types of actuators are available. The first type is piezoelectric actuators, which have advantages of high control bandwidth, high force and small size [25]. For these reasons, piezos are commonly used in AFMs. However, these actuators have a high stiffness between the moving

and end pieces. Because this high stiffness strongly transmits the floor vibrations impairing the positioning resolution, piezoelectric actuators are not suitable for vibration isolation systems (cf. high stiffness actuators [26]).

The second actuator type is Lorentz actuators (or voice coil actuators), which are composed of coils and permanent magnets for the Lorentz force. When a small size is required, their movers are guided by flexures [27]. Because the actuation principle itself does not add stiffness, the stiffness between the mover and the stator is determined by the flexure design. Particularly by designing a flexure-guided actuation system, such that its suspension mode occurs at a frequency sufficiently smaller than the closed-loop control bandwidth, it can combine active vibration rejection and passive vibration isolation for high-precision positioning [26]. Such a positioning system can attain immunity against the floor vibrations and can be referred to as “low stiffness actuator” [26]. Since the characteristics of the low stiffness actuator are ideal for the proposed system, flexure-guided Lorentz actuators are selected as the Z-axis vibration rejection actuators.

For the proposed system, four identical Lorentz actuators with flat coils (AVA-1-20-0.5, Akribis Systems, Singapore) are selected. A photograph of one of them is shown in Fig. 4, where the magnet assembly consists of pairs of permanent magnets, and the flat coil is inserted in the magnets’ gap for the Lorentz force [7]. To reserve the space on the moving platform’s base plate for the AFM head, the moving flat coils are attached on the sides as shown in Fig. 3, where the red arrows denote the actuation force. The magnet assemblies are attached to the fixed base (cf. Fig. 8). For over-actuation [28], four Lorentz actuators are used for the Z-axis motion. By tuning the force balance of these actuators, the resulting force can be applied at the center of gravity of the platform with the AFM head to be integrated. As a result, the platform can vertically move without exciting its rotational modes, which is beneficial to achieve a high control bandwidth [17]. The selected actuators have a nominal motor constant of  $K_m = 1.37 \text{ N/A}$ .

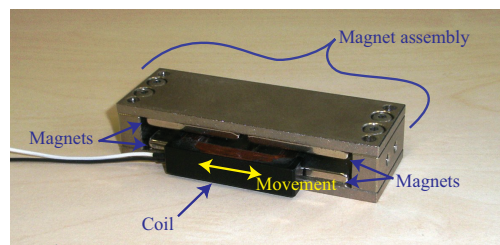


Figure 4: Photograph of a selected Lorentz actuator where the coil is inserted between the magnets for the Lorentz force.

### 3.3. Actuator amplifiers

For the previously selected actuators, four identical current amplifiers are developed because the Lorentz force is proportional to the coil current. Each current amplifier has an internal feedback controller and current monitor to regulate the output current up to 2 A. Fig. 5 shows a block diagram of the closed loop, where one of the Lorentz actuators is modeled

as a transfer function from the voltage over the coil  $V$  to the coil current  $I$

$$\frac{I(s)}{V(s)} = \frac{1}{Ls + R}, \quad (1)$$

where  $R = 1.5 \Omega$  and  $L = 0.26 \text{ mH}$  are the resistance and inductance of the coil, respectively. Proportional to the velocity of the coil with respect to the magnets, the back electromotive force (EMF)  $V_{EMF}$  is generated as the disturbance in the closed loop. However, since the Lorentz actuator's stroke is too short to have a high velocity, the back EMF can be neglected in the control design.

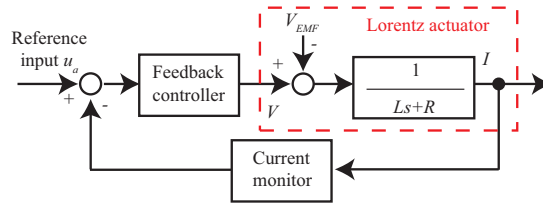


Figure 5: Block diagram of a current amplifier with a Lorentz actuator.

Because (1) is only first order, a PI controller is sufficient and implemented for feedback control. Its internal gains are tuned to achieve a bandwidth of more than several kilohertz. The current amplifiers are implemented by operational amplifiers (OPA544, OPAx277, Texas Instruments, Dallas, USA) and passive components without a digital control circuit in order to prevent a delay and quantization noise. For validation, a frequency response is measured from the input voltage  $u_a$  to the current  $I$  as shown in Fig. 6, where  $u_a$  is scaled to Ampere by the amplifier gain  $200 \text{ mA/V}$ . As desired, a relatively flat magnitude and phase can be seen up to about  $500 \text{ Hz}$ . The  $-3 \text{ dB}$  bandwidth of the amplifier is  $20 \text{ kHz}$  for the actuation, satisfying the requirements in Section 2.3. Since the Lorentz force is proportional to the coil current, each Lorentz actuator with the designed current amplifier can generate the maximum force of  $2.74 \text{ N}$  with the  $-3 \text{ dB}$  bandwidth of  $20 \text{ kHz}$ .

For the over-actuation discussed in the previous section, the force balance of the four actuators can be adjusted by changing each amplifier's gain. In this implementation, however, the gain of all the current amplifiers are set to  $K_a = 200 \text{ mA/V}$  because the center of gravity of the developed moving platform occurs around the center part between the actuators. By using the internal current monitor, the output current is measured for evaluation, and its noise is determined as a small value of  $60 \mu\text{A}_{\text{rms}}$ .

### 3.4. Displacement sensor

In addition to the bandwidth as discussed in Section 2.3, the displacement sensor needs to have sufficiently small measurement noise for a high signal-to-noise ratio. It is also desired that the sensor is small enough to integrate with the moving platform. Therefore, a fiber-optic displacement sensor (ATW-01/ATP-A20, Unipulse, Tokyo, Japan) is selected. The calibrated sensor has a sensitivity  $K_s$  of  $0.341 \text{ mV/nm}$  with a measurement range of about  $30 \mu\text{m}$ .

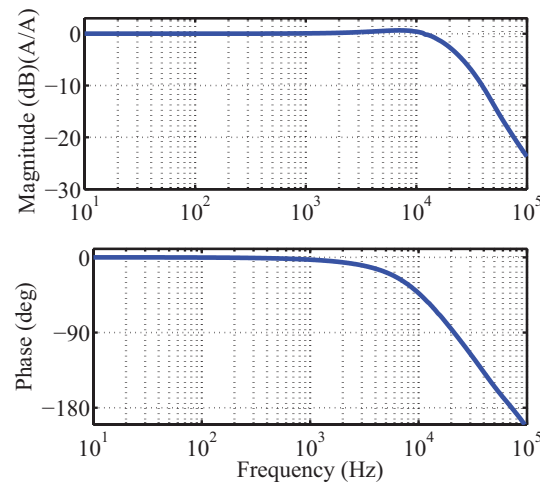


Figure 6: Measured Bode plot of a current amplifier from the input voltage  $u_a$  to the output current  $I$ . The signal  $u_a$  is scaled to Ampere by the amplifier gain 200 mA/V.

Table 1: Measured noise of displacement sensor for 100 kHz bandwidth.

Sensor target	Silicon wafer	Petro wax	Polymer
Noise (nm <sub>rms</sub> )	2.0	9.5	8.3

The displacement sensor has the additional advantage of non-contact measurement. Furthermore, its sensitivity is independent of the sensor target's reflectivity. Due to these properties, if the AFM sample is large (Fig. 1), the sensor may be used to directly measure the distance to the sample. However, in that case, the reflectivity of the target may influence the measurement noise, which may dominate the achievable vibration rejection performance. Therefore, the measurement noise of the sensor is evaluated with three different targets: a reflective unprocessed silicon wafer, opaque petro wax (080A109, PCB, Depew, USA) and transparent polymer (Sylguard 184, Dow Corning, Midland, USA). The wax and polymer are prepared on a glass substrate. By considering the requirements in Section 2.3, the sensor bandwidth is set to a sufficiently high frequency of 100 kHz. While noise below 10 nm is achieved in all three cases as listed in Table 1, it is relatively large with the wax and the polymer. This noise may be reduced in a trade-off with the achievable sensor bandwidth [13], depending on the application. For the experimental demonstration in this paper, a silicon wafer is used as the sensor target, with sensor bandwidth of 100 kHz.

### 3.5. AFM head

As the AFM head for the experimental demonstration of the proposed system, a commercial AFM (afm+, Anasys, Santa Barbara, USA) is used for its compact size, in combination with its data acquisition system. The AFM head of the commercial AFM is 250 g, including the AFM probe, the deflection sensor and the Z-axis actuator. By using permanent magnets, the AFM head is attached on top of the platform's base plate (Fig. 3).

### 3.6. Flexure design

As introduced in Section 3.2, flexures are used to guide the moving platform along the Z axis. In this case, the suspension mode occurs at the natural frequency  $\omega_n$

$$\omega_n = \sqrt{k/m}, \quad (2)$$

where  $m$  is the overall mass of the moving platform including the sub-components, and  $k$  is the total stiffness of the flexures along the actuation axis. Compact high-precision actuators usually have a damping that is way smaller than the critical damping resulting in a high resonance peak at  $\omega_n$  [26]. While this resonance peak is typically regarded as an unwanted property in passive vibration isolators or piezo-actuated systems [29], it is beneficial with low stiffness actuators to increase the open-loop gain for control, enabling better vibration rejection at this frequency [26]. Because the high vibration rejection is required up to 30 Hz in Section 2.3, the flexures are designed to set  $\omega_n$  at round that frequency.

Leaf-spring flexures are selected to guide the moving platform because they are ideal to make flexures with low stiffness [25]. By using Castigliano's second theorem [30] or the bending moment [31], the stiffness  $k_f$  of a single leaf-spring flexure is related to its dimension and the Young's modulus  $E$  of the material as follows

$$k_f = Ewh^3/L^3, \quad (3)$$

where  $w$ ,  $h$  and  $L$  are the width, height and length of the flexures as shown in Fig. 7. By considering the number  $n_f$  of the flat-spring flexures for guiding, the resulting natural frequency can be obtained from (2) and (3) as

$$\omega_n = \sqrt{\frac{n_f k_f}{m}} = \sqrt{\frac{n_f Ewh^3}{mL^3}}. \quad (4)$$

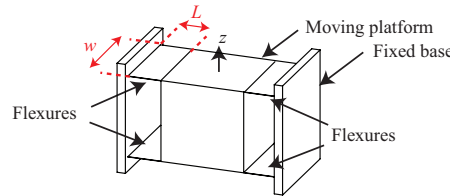


Figure 7: Illustration of the moving platform guided by leaf-spring flexures, where  $w$  and  $L$  are the width and length of the flexures, respectively.

To use (4) for flexure design,  $m$  is roughly estimated as 1.1 kg from the 3D model of the moving platform, together with the mass of the Lorentz coils and the AFM head. Aluminum is selected for the flexures, providing  $E = 68$  GPa. With these values, the flexure dimension and number are determined, such that  $\omega_n$  takes a value close to 30 Hz. The determined values are listed in Table 2, based on which the flexures are manufactured by cutting aluminum sheets of 0.5 mm. As shown in Fig. 3, the flexures are clamped and attached to the moving platform.

Table 2: Design parameters of flexures.

Parameter	Value
$L$	40 mm
$w$	104 mm
$h$	0.5 mm
$n_f$	4
$\omega_n$	35.7 Hz

### 3.7. Overall system assembly

As shown in Fig. 8, the manufactured moving platform is assembled with the fixed base. On the XY scanner (NPXY100-100, nPoint, Middleton, USA) for the sample scanning, a Z-axis manual stage is placed for the AFM tip engagement. The stage mounts a calibration grating of 114 nm height (HS-100MG, Innovative Solutions, Sofia, Bulgaria) as a test sample for AFM imaging. Notice that the assembled AFM system has a long mechanical loop from the sample to the AFM probe, due to a relatively large distance (220 mm) between the mechanical supports, as indicated in Fig. 8(b).

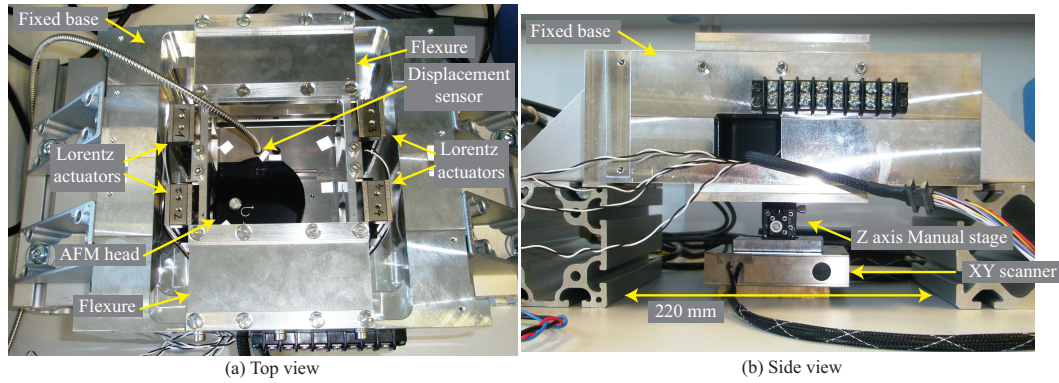


Figure 8: Photographs of the vibration isolation system: (a) top view and (b) side view.

## 4. System analysis

### 4.1. Modeling

The assembled system can be modeled for the Z axis actuation as shown in Fig. 9, where  $z_b$ ,  $z_m$  and  $z_s$  are the vertical position of the fixed base, the moving platform and the XY stage, respectively. An equation of motion is derived as follows

$$m\ddot{z}_m(t) + c\{\dot{z}_m(t) - \dot{z}_b(t)\} + k\{z_m(t) - z_b(t)\} = F(t), \quad (5)$$



where  $c$  and  $k$  are the total damping and the stiffness of the flexures, respectively, as well as the total mass  $m$  of the moving platform. Since the sum of the actuation force  $F$  is proportional to the coil current  $I$ , it is given as

$$F(t) = \sum_{i=1}^{n_a} K_m I(t) = n_a K_m K_a u_a(t), \quad (6)$$

where  $n_a = 4$  and  $K_m$  are the number and the motor constant of the Lorentz actuators, respectively. The other parameters  $K_a$  and  $u_a$  are the gain and the input voltage of the current amplifiers, respectively. Since the displacement sensor measures the distance between the moving platform and the XY stage, its output signal  $y$  is given as

$$y(t) = K_s(z_m(t) - z_s(t)), \quad (7)$$

where  $K_s$  is the sensor sensitivity. After the Laplace transformation, the sensor output  $Y(s)$  is represented by

$$Y(s) = P_a(s)n_a K_m K_a K_s U_a(s) + K_s P_t(s) Z_b(s) - K_s Z_s(s), \quad (8)$$

using the following transfer functions

$$P_a(s) = \frac{Z_m(s)}{F(s)} = \frac{1}{ms^2 + cs + k} = \frac{1/k}{\frac{s^2}{\omega_n^2} + 2\zeta\frac{s}{\omega_n} + 1}, \quad (9)$$

$$P_t(s) = \frac{Z_m(s)}{Z_b(s)} = \frac{cs + k}{ms^2 + cs + k} = \frac{2\zeta\frac{s}{\omega_n} + 1}{\frac{s^2}{\omega_n^2} + 2\zeta\frac{s}{\omega_n} + 1}, \quad (10)$$

where  $U_a(s)$ ,  $Z_b(s)$  and  $Z_s(s)$  are the Laplace transform of  $u_a$ ,  $z_b$  and  $z_s$ , respectively, and  $\zeta$  is the damping ratio given by  $c/(2\sqrt{km})$ . The transfer function  $P_t(s)$  is the transmissibility, determining the transmission of the vibration  $z_b$  to the moving platform.

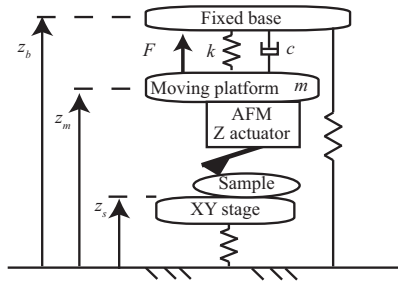


Figure 9: Lumped mass model of the vibration isolation system.

From (8)-(10), the derived model can be visualized by a block diagram in Fig. 10, where  $z_b$  and  $z_s$  are regarded as vibrational disturbances. These disturbances are rejected to maintain

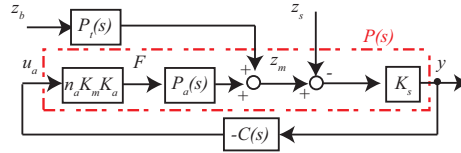
Table 3: Estimated plant parameters for control design and analysis.

Parameter	Value
$g_p$	13.4
$\omega_n$	$2\pi \cdot 34.7$ rad/s
$\zeta$	0.025

the distance between  $z_m$  and  $z_s$  by a feedback controller  $C(s)$  to be designed. For the design of  $C(s)$ , the transfer function  $P(s)$  from the input voltage  $u_a$  to the output  $y$  is derived as

$$P(s) = \frac{Y(s)}{U_a(s)} = n_a K_m K_a K_s P_a(s) = \frac{g_p}{\frac{s^2}{\omega_n^2} + 2\zeta \frac{s}{\omega_n} + 1}, \quad (11)$$

where  $g_p = n_a K_m K_a K_s / k$  is the plant gain.

Figure 10: Block diagram of the vibration isolation system with feedback controller  $C(s)$ .

#### 4.2. Frequency response

Using a network analyzer (3562A, Hewlett Packard, Palo Alto, USA), a Bode plot of the mechatronic system from  $u_a$  to  $y$  is measured as shown in Fig. 11. In the magnitude plot, a peak due to the suspension mode can be seen around 30 Hz, as intended in the flexure design of Section 3.6. Beyond that frequency, a line with a slope of -40 dB/dec, referred to as “mass-line” [7], is visible up to a high frequency of about 1 kHz. Also, notice that the phase in this range is almost constant near -180 deg without a phase lag or delay up to 1 kHz, as intended in the amplifier development and the selection of the displacement sensor. Parasitic dynamics can be seen beyond 1 kHz, which may be due to mechanical resonances of components, such as the Lorentz coils, the AFM head and the flexures.

The damping  $c$  is unknown, and  $m$  is roughly estimated for mechanical design. Furthermore,  $k$  is influenced by the machining tolerance. Thus, the model parameters  $\omega_n$ ,  $\zeta$  and  $g_p$  are experimentally determined based on the measured frequency response for the reduction of modeling uncertainties in the control design. Those parameters are tuned, such that the frequency response of the resulting model  $P(s)$  in (11) accord with the measured response, as shown in Fig. 11. The determined parameters are listed in Table 3.

## 5. Control design

### 5.1. Design

In order to design a high-precision positioning system with immunity against floor vibrations as a low stiffness actuator, its feedback controller  $C(s)$  must realize a control bandwidth

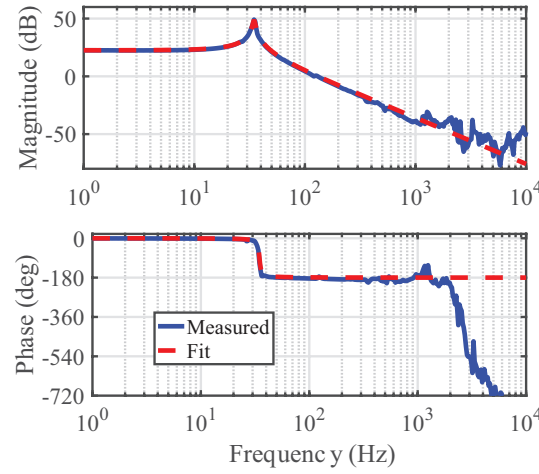


Figure 11: Measured Bode plot from  $u_a$  to  $y$  and the plant model (11) fit to the measured data.

sufficiently higher than  $\omega_n$  [26]. Because the Bode plot in Fig. 11 shows a phase of -180 deg beyond  $\omega_n$ ,  $C(s)$  is required to provide a sufficient phase lead at a desired open-loop cross-over frequency  $\omega_c$ . Furthermore, to utilize the mechanical mode at  $\omega_n$  for vibration rejection as intended in Section 3.6,  $C(s)$  must not cancel the plant poles of the mode [26]. Satisfying these controller requirements, a PID controller with a first-order low-pass filter is selected as  $C(s)$ .

The PID controller is configured as a phase-lead compensator combined with a PI controller of the corner frequency  $\omega_z$ , to provide a phase lead for stability [24] as follows

$$C(s) = g_c \left( 1 + \frac{\omega_z}{s} \right) \left( \frac{\alpha s + \omega_c}{s + \omega_c \alpha} \right), \quad (12)$$

where  $g_c$  is the controller gain set to  $\omega_c^2/(g_p \omega_n^2)$ , such that  $|C(s)P(s)|$  intersects the 0 dB line at the desired open-loop cross-over frequency  $\omega_c$ . The parameter  $\alpha$  determines the phase lead  $\phi$  given by the lead compensator parts at  $\omega_c$  [32]

$$\phi = \sin^{-1} \left( \frac{\alpha^2 - 1}{\alpha^2 + 1} \right). \quad (13)$$

Because the PI controller introduces a phase lag reducing the achievable phase lead of  $C(s)$ ,  $\omega_z$  needs to be sufficiently smaller than  $\omega_c$ . As a rule of thumb [7],  $\omega_z$  and  $\alpha$  are set to  $0.1\omega_c$  and 3, respectively. Because the resonance peak at 1.3 kHz restricts the closed bandwidth and decreases the gain margin,  $\omega_c$  is set to  $2\pi \cdot 450$  rad/s for closed-loop stability. The parameter values of the designed controller are listed in Table. 4.

## 5.2. Analysis

For the reduction of the modeling uncertainty in the control design, the plant parameters are experimentally estimated. However, there is a possibility that the stiffness  $k$  varies when

Table 4: Parameters of  $C(s)$  in (12)

Parameter	Value
$g_c$	12.5
$\omega_c$	$2\pi \cdot 450 \text{ rad/s}$
$\omega_z$	$2\pi \cdot 45 \text{ rad/s}$
$\alpha$	3

the flexures are significantly deformed. Although high-precision positioning systems with flexures are typically operated in a short stroke for the flexures' linearity [22], influence of the stiffness variation is analyzed to demonstrate capabilities of the proposed AFM system in this section.

For the analysis, a scale factor  $\Delta_k$  of the stiffness  $k$  is introduced as an uncertainty to the plant gain  $g_p$  as follows

$$g_{p,\Delta}(\Delta_k) = \frac{n_a K_m K_a K_s}{k \Delta_k} = \frac{g_p}{\Delta_k}. \quad (14)$$

Similarly, the natural frequency and the damping ratio can include the stiffness uncertainty

$$\omega_{n,\Delta}(\Delta_k) = \omega_n \sqrt{\Delta_k}, \quad \zeta_{\Delta}(\Delta_k) = \zeta / \sqrt{\Delta_k}. \quad (15)$$

By replacing  $g_p$ ,  $\omega_n$  and  $\zeta$  by  $g_{p,\Delta}$ ,  $\omega_{n,\Delta}$  and  $\zeta_{\Delta}$  in (11), the open-loop transfer function  $P(s)C(s)$  is simulated by varying  $\Delta_k$  within a relatively large range from 50 % to 150 % with a 10 % step.

The results in Fig. 12 show that the stiffness variation only influences the response around the first resonant frequency and below. Consequently, the magnitude plot crosses the 0 dB line around 450 Hz, as specified by  $\omega_c$  in the control design. The phase plot at that frequency is -132 deg, and the phase margin is 47 degrees, regardless of the stiffness variation, as required in Section 2.3. This is because the -40 dB/dec line seen beyond the first resonant frequency  $\omega_n$  in Fig. 11 is not influenced by  $k$ . Thus, by setting  $\omega_c$  to a frequency sufficiently higher than  $\omega_n$ , the proposed AFM system is robust stable against the stiffness variation.

When the designed  $C(s)$  is applied to reject vibrations as shown in Fig. 10, the residual vibrations  $z_m - z_s$  can be derived by replacing  $U_a(s)$  by  $-C(s)Y(s)$  in (8) as follows

$$Z_m(s) - Z_s(s) = Y(s)/K_s = S(s)P_t(s)Z_b(s) - S(s)Z_s(s), \quad (16)$$

where  $S(s)$  is the sensitivity function  $(1 + C(s)P(s))^{-1}$ . Because  $S(s)$  quantifies the rejection of  $z_s$  in (16) and also influences that of  $z_b$ ,  $S(s)$  is also simulated by varying  $\Delta_k$  from 50 % to 150 % with a 10 % step. The black dotted lines in Fig. 13(a) show the results. The simulation indicates that the designed controller can reject  $Z_s(s)$  up to about 300 Hz, regardless of the stiffness variation, as required in Section 2.3. Furthermore, the vibration rejection is improved by a notch seen around 30 Hz dependent on  $\Delta_k$ . This is because the first mechanical resonance increases the gain of the open-loop transfer function (cf. Fig. 12), as intended in the mechanical and the control design for better vibration rejection.

The term  $S(s)P_t(s)$  in (16) is the transfer function from  $z_b$  to  $z_m$  and quantifies the transmission of the vibration  $z_b$  to the moving platform while feedback controller is active.

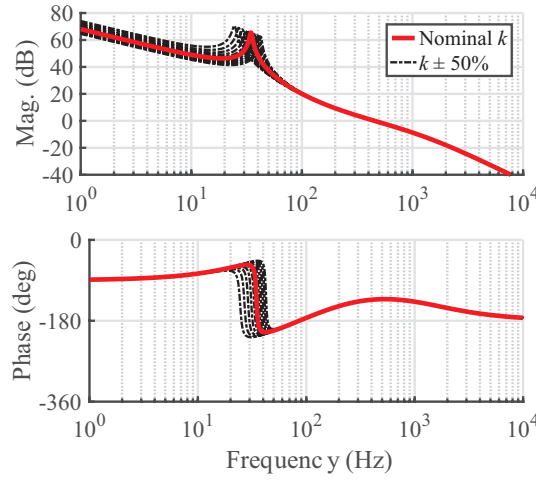


Figure 12: Simulated open-loop transfer function  $C(s)P(s)$  by varying the stiffness between 50 % and 150 % with a 10 % step.

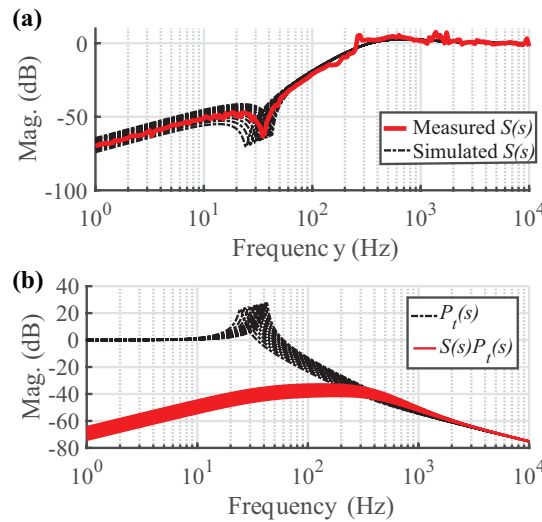


Figure 13: Frequency response of (a) sensitivity function  $S(s)$ , (b) passive transmissibility  $P_t(s)$  and active transmissibility  $S(s)P_t(s)$ . For the simulation of  $S(s)$ ,  $P_t(s)$  and  $S(s)P_t(s)$ , the stiffness is varied from 50 % and 150 % with a 10 % step. Additionally,  $S(s)$  is experimentally measured for validation.

Thus, it is defined as the active transmissibility. For analysis the active transmissibility  $S(s)P_t(s)$  and the passive transmissibility  $P_t(s)$  are simulated by varying  $\Delta_k$  from 50 % to 150 % with a 10 % step in Fig. 13(b). The simulated  $P_t(s)$  without feedback control shows a magnitude smaller than 0 dB at a frequency higher than  $\sqrt{2}\omega_{n,\Delta}$ , which is the mechanical vibration isolation of the low-stiffness actuator. However,  $P_t(s)$  has a gain peak around the

first resonant frequency, where the moving platform is strongly excited by  $z_b$ .

The strong excitation of the resonant mode is no longer a problem by turning on the controller  $C(s)$ . This is clearly visible in the plot of  $S(s)P_t(s)$ , where the gain peak of  $P(s)$  is perfectly trimmed by the notch of  $S(s)$ , regardless of the stiffness variation. More importantly,  $S(s)P_t(s)$  shows a magnitude sufficiently smaller than 0 dB for the entire frequency range. This is because the designed low-stiffness actuator can smoothly combine the active vibration rejection up to about 300 Hz with the passive vibration isolation from 60 Hz in Fig. 13(b). Such active transmissibility for high vibration immunity can be realized only if the natural frequency  $\omega_n$  is sufficiently lower than the open-loop cross-over frequency  $\omega_c$  [26].

In summary, the robustness analysis reveals that the resulting closed-loop AFM system is robust stable against the stiffness variation. Furthermore, the proposed AFM system combines the active rejection and the passive isolation to handle the vibration  $z_b$  and uses the first resonant mode to better reject the disturbance  $z_s$ . Even if the stiffness  $k$  greatly varies, the proposed AFM system holds these properties.

### 5.3. Validation

The designed and analyzed PID controller is implemented by an analog circuit with operational amplifiers [33] since it does not contain quantization noise unlike a typical digital filter. For the validation, the sensitivity function  $S(s)$  is measured, as shown by the red solid line in Fig. 13(a). The -3 dB bandwidth of the sensitivity function is 251 Hz, satisfying the requirements in Section 2.3. The plot also shows a deep notch at about 35 Hz due to the high gain of the suspension mode. Consequently, the plot shows a steep line between 40 Hz and 60 Hz, resulting in a small magnitude at the lower frequencies. Particularly below 30 Hz, the magnitude is smaller than -45 dB for high vibration rejection, as required in Section 2.3. The measured sensitivity function demonstrates the successful utilization of the mechanical suspension mode for vibration rejection.

## 6. Experiments

### 6.1. Vibration rejection

In order to evaluate the performance of the vibration isolation system, the distance between the moving platform and the XY scanner (i.e. the vibrations that affect the AFM imaging) is measured by the displacement sensor while the feedback control is turned on and off. The mean value is subtracted from the recorded data because it does not influence the AFM imaging quality. When the feedback control is turned off in Fig. 14(a), the distance fluctuates about  $\pm 1000$  nm. From these data, the RMS value is calculated as  $358 \text{ nm}_{\text{rms}}$ . In the case that the feedback control is turned on (Fig. 14(b)), the residual vibrations are reduced to a range of about  $\pm 10$  nm. The calculated RMS is  $2.48 \text{ nm}_{\text{rms}}$ , which means that the vibration isolation system rejects 99.3 % of the vibrations, providing a quiet environment for AFM imaging.

### 6.2. AFM imaging

In order to demonstrate AFM imaging, the data acquisition system and the control electronics of the commercial AFM are used. For the Z axis actuation of the AFM probe, the internal feedback controller is configured as an integral controller, such that it can be tuned



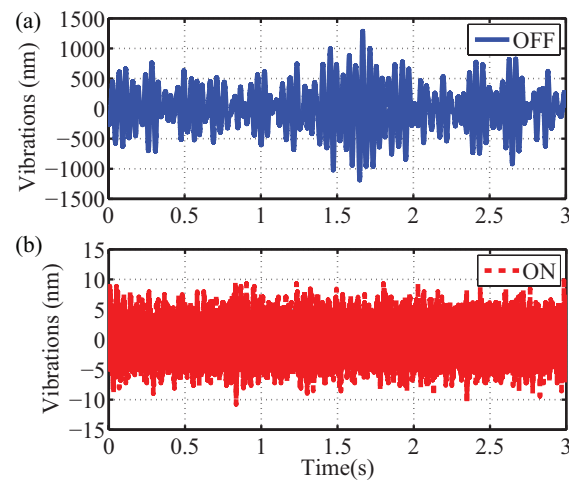


Figure 14: Distance between the moving platform and the XY scanner measured as vibrations by the displacement sensor when the feedback control is (a) turned off and (b) turned on. Note that the scaling of the two signals differs by a factor of 100.

without system identification [1, 34]. The integral gain is maximized in the beginning of each experiment within a domain that assures closed-loop stability. The 114 nm calibration grating is used as the sample, which is scanned by the XY scanner with a triangle signal of 2 Hz for the fast scanning axis.

For comparison, AFM images are obtained when the feedback control is turned off and on, as shown in Fig. 15. In the case that the control is turned off, the topography and deflection images in Fig. 15(a)(b) are dominated by grainy stripes due to vibrations. Consequently, it is impossible to clearly measure topography of the sample features although the main structure might be guessed in the noise. This is more clearly seen with the single line profile in Fig. 15(c), where the 114 nm height cannot be distinguished from the vibrations of about  $\pm 250$  nm. The AFM is useless as a measurement tool due to the vibrations when the vibration rejection is inactive.

When the feedback control is activated, however, the disturbances due to vibrations are eliminated in the topography and deflection images of Fig. 15(d)(e). As a result, the circular features of the sample can clearly be resolved in Fig. 15(d). In the single line profile of the topography in Fig. 15(e), the height and the width of the features can be identified, demonstrating that by using the vibration isolation system the AFM functions properly as an imaging tool.

Overall, the experimental results clearly demonstrate that the proposed compact system can reject vibrations for AFM imaging in vibrational environments that are unsuitable for high-precision imaging, as evaluated in Section 2.2. The demonstrated properties may enable on-site AFM imaging, and its potential application includes AFM imaging of marine bacteria [35] on a boat, as well as AFM imaging of products next to or in a production line to increase the production reliability (i.e. online or inline metrology [36]).

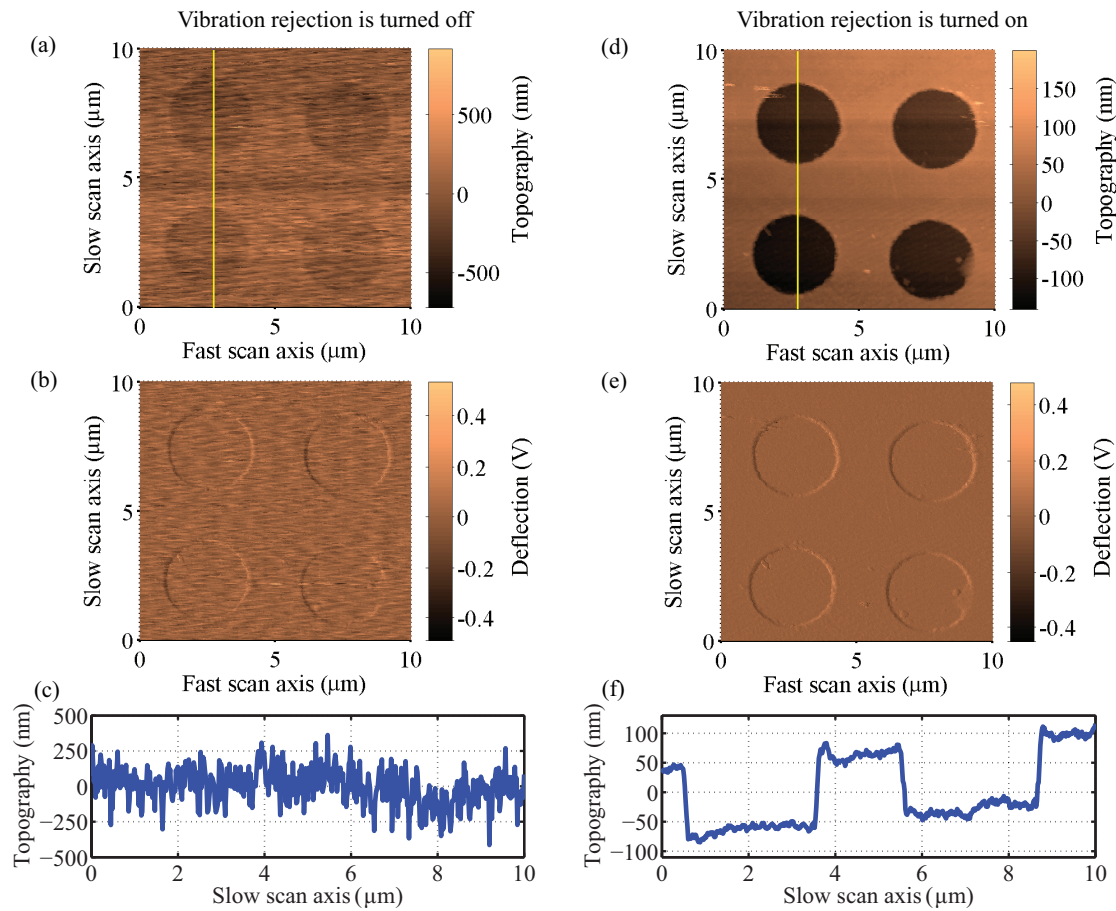


Figure 15: AFM images measured when the feedback control is (a-c) turned off and (d-f) on, showing (a)(d) topography images, (b)(e) deflection images. The yellow lines in (a) and (d) represent the sampled data set for the single line profiles in (c)(f).

## 7. Conclusion and future work

This paper presents the overall mechatronic system design of the positioning system carrying an AFM head for vibration isolation. While the moving platform is mechanically guided by flexures, the Lorentz actuators have been selected to achieve high vibration isolation performance. The proposed system utilizes the suspension mode, which has been adjusted by the flexure design to improve the vibration isolation performance. Rejection of vibrations is achieved by feedback control based on measurement by the high-bandwidth displacement sensor. The experimental results show that the proposed system rejects 99.3 % of the vibrations by activating its feedback controller. As a result, successful AFM imaging is demonstrated in harsh environments. Future work includes development of an AFM system for online or inline metrology.

## Acknowledgments

This work has been supported in part by the Austrian Research Promotion Agency (FFG) under project number 836489, and in part by the Austrian Federal Ministry of Science, Research and Economy and the National Foundation for Research, Technology and Development, as well as MICRO-EPSILON MESSTECHNIK GmbH & Co. KG and ATENSOR Engineering and Technology Systems GmbH.

## References

- [1] P. Eaton, P. West, Atomic Force Microscopy, Oxford University Press, 2010.
- [2] E. Meyer, H. J. Hug, R. Bennewitz, Scanning Probe Microscopy, Springer-Verlag Berlin Heidelberg, 2004.
- [3] H. Amick, M. Gendreau, T. Busch, C. Gordon, Evolving criteria for research facilities I: vibration, in: Proc. SPIE 5933, Vol. 5933, 2005, p. 593303. doi:10.1117/12.617970.
- [4] H. Amick, D. H. Sturz, E. E. Ungar, Vibration control design of high technology facilities, Sound and Vibration - (1990) 20–27.
- [5] M. O. Al-Hunaidi, J. H. Rainer, M. Tremblay, Control of traffic-induced vibration in buildings using vehicle suspension systems, Soil Dynamics and Earthquake Engineering 15 (4) (1996) 245–254. doi:10.1016/0267-7261(95)00047-X.
- [6] H. Xia, N. Zhang, Y. M. Cao, Experimental study of train-induced vibrations of environments and buildings, Journal of Sound and Vibration 280 (35) (2005) 1017–1029. doi:10.1016/j.jsv.2004.01.006.
- [7] R. Munnig Schmidt, G. Schitter, A. Rankers, J. van Eijk, The Design of High Performance Mechatronics, 2nd Edition, Delft University Press, 2014.
- [8] Q. Li, Y. Zhu, D. Xu, J. Hu, W. Min, L. Pang, A negative stiffness vibration isolator using magnetic spring combined with rubber membrane, Journal of Mechanical Science and Technology 27 (3) (2013) 813–824. doi:10.1007/s12206-013-0128-5.
- [9] G. Balik, B. Caron, J. Allibe, A. Badel, J.-P. Baud, L. Brunetti, G. Deleglise, A. Jeremie, R. Le Breton, S. Vilalte, Sub-nanometer active seismic isolator control, Journal of Intelligent Material Systems and Structures 24 (15) (2013) 1785–1795. doi:10.1177/1045389X13500571.
- [10] D. Kohl, D. Mick, R. Saathof, G. Schitter, Extending the range of geophone by negative impedance converter, in: 7th IFAC Symposium on Mechatronic Systems (IFAC-PapersOnLine), Vol. 49, 2016, pp. 541–546. doi:10.1016/j.ifacol.2016.10.658.
- [11] C. Collette, F. Matichard, Sensor fusion methods for high performance active vibration isolation systems, Journal of Sound and Vibration 342 (2015) 1–21. doi:10.1016/j.jsv.2015.01.006.

- [12] J. H. Kindt, G. E. Fantner, J. A. Cutroni, P. K. Hansma, Rigid design of fast scanning probe microscopes using finite element analysis, *Ultramicroscopy* 100 (34) (2004) 259–265. doi:10.1016/j.ultramic.2003.11.009.
- [13] A. J. Fleming, A review of nanometer resolution position sensors: Operation and performance, *Sensors and Actuators A: Physical* 190 (2013) 106–126. doi:10.1016/j.sna.2012.10.016.
- [14] G. Schitter, A. Stemmer, Eliminating mechanical perturbations in scanning probe microscopy, *Nanotechnology* 13 (5) (2002) 663–665. doi:10.1088/0957-4484/13/5/324.
- [15] A. W. Sparks, S. R. Manalis, Atomic force microscopy with inherent disturbance suppression for nanostructure imaging, *Nanotechnology* 17 (6) (2006) 1574–1579. doi:10.1088/0957-4484/17/6/007.
- [16] C. Kim, J. Jung, K. Park, Note: Vibration reduction control of an atomic force microscope using an additional cantilever, *Review of Scientific Instruments* 82 (11) (2011) –. doi:10.1063/1.3660776.
- [17] S. Ito, D. Neyer, S. Pirker, J. Steininger, G. Schitter, Atomic force microscopy using voice coil actuators for vibration isolation, in: *IEEE/ASME International Conference on Advanced Intelligent Mechatronics*, 2015, pp. 470–475. doi:10.1109/AIM.2015.7222578.
- [18] S. Ito, J. Steininger, G. Schitter, Low-stiffness dual stage actuator for long range positioning with nanometer resolution, *Mechatronics* 29 (2015) 46–56. doi:10.1016/j.mechatronics.2015.05.007.
- [19] A. J. Fleming, Dual-stage vertical feedback for high-speed scanning probe microscopy, *IEEE Transactions on Control Systems Technology* 19 (1) (2011) 156–165. doi:10.1109/TCST.2010.2040282.
- [20] B. J. Kenton, A. J. Fleming, K. K. Leang, Compact ultra-fast vertical nanopositioner for improving scanning probe microscope scan speed, *Review of Scientific Instruments* 82 (12) (2011) 123703. doi:10.1063/1.3664613.
- [21] S. Kuiper, G. Schitter, Model-based feedback controller design for dual actuated atomic force microscopy, *Mechatronics* 22 (3) (2012) 327–337. doi:10.1016/j.mechatronics.2011.08.003.
- [22] T. Tuma, W. Haeberle, H. Rothuizen, J. Lygeros, A. Pantazi, A. Sebastian, Dual-stage nanopositioning for high-speed scanning probe microscopy, *IEEE/ASME Transactions on Mechatronics* 19 (3) (2014) 1035–1045. doi:10.1109/TMECH.2013.2266481.
- [23] L. Jabben, Mechatronic design of a magnetically suspended rotating platform, Ph.D. thesis, Technische Universiteit Delft (2007).
- [24] T. Yamaguchi, M. Hirata, C. Pang, *High-Speed Precision Motion Control*, Taylor & Francis, 2011.

- [25] Y. K. Yong, S. O. R. Moheimani, B. J. Kenton, K. K. Leang, Invited review article: High-speed flexure-guided nanopositioning: Mechanical design and control issues, *Review of Scientific Instruments* 83 (12) (2012) –. doi:10.1063/1.4765048.
- [26] S. Ito, G. Schitter, Comparison and classification of high-precision actuators based on stiffness influencing vibration isolation, *IEEE/ASME Transactions on Mechatronics* 21 (2) (2016) 1169–1178. doi:10.1109/TMECH.2015.2478658.
- [27] S. Kim, M. G. Song, N. C. Park, J. Yoo, Y. P. Park, K. S. Park, Optimal design of moving-magnet type actuators for optical disk drives considering effect of coil electromagnet, *IEEE Transactions on Magnetics* 45 (5) (2009) 2228–2231. doi:10.1109/TMAG.2009.2016164.
- [28] M. J. C. Ronde, M. G. E. Schneiders, E. J. G. J. Kikken, M. J. G. van de Molengraft, M. Steinbuch, Model-based spatial feedforward for over-actuated motion systems, *Mechatronics* 24 (4) (2014) 307 – 317.
- [29] A. J. Fleming, Nanopositioning system with force feedback for high-performance tracking and vibration control, *IEEE/ASME Transactions on Mechatronics* 15 (3) (2010) 433–447. doi:10.1109/TMECH.2009.2028422.
- [30] B. J. Kenton, K. K. Leang, Design and control of a three-axis serial-kinematic high-bandwidth nanopositioner, *IEEE/ASME Transactions on Mechatronics* 17 (2) (2012) 356–369. doi:10.1109/TMECH.2011.2105499.
- [31] S. Ito, F. Cigarini, S. Unger, G. Schitter, Flexure design for precision positioning using low-stiffness actuators, in: 7th IFAC Symposium on Mechatronic Systems (IFAC-PapersOnLine), Vol. 49, 2016, pp. 200–205. doi:10.1016/j.ifacol.2016.10.548.
- [32] W. C. Messner, M. D. Bedillion, L. Xia, D. C. Karns, Lead and lag compensators with complex poles and zeros design formulas for modeling and loop shaping, *IEEE Control Systems Magazine* 27 (1) (2007) 44–54. doi:10.1109/MCS.2007.284508.
- [33] P. Horowitz, W. Hill, *The Art of Electronics*, 3rd Edition, Cambridge University Press, 2015.
- [34] D. Kohl, T. Riel, R. Saathof, J. Steininger, G. Schitter, Auto-tuning PI controller for surface tracking in atomic force microscopy - a practical approach, in: American Control Conference, 2016, pp. 7396–7401. doi:10.1109/ACC.2016.7526840.
- [35] T. Nishino, E. Ikemoto, K. Kogure, Application of atomic force microscopy to observation of marine bacteria, *Journal of Oceanography* 60 (2) (2004) 219–225. doi:10.1023/B:JOCE.0000038328.54339.e4.
- [36] R. Schmitt, F. Moenning, Ensure success with inline-metrology, in: IMEKO World Congress, 2006.